Triboelectric Polymer with High Thermal Charge Stability for Harvesting Energy from 200 °C Flowing Air

Xinglin Tao, Shuyao Li, Yuxiang Shi, Xingling Wang, Jingwen Tian, Zhaoqi Liu, Peng Yang, Xiangyu Chen, and Zhong Lin Wang*

Due to the thermionic emission effect, the electron transferred to dielectric surface can be released into vacuum after the contact electrification (CE). Therefore, triboelectric nanogenerator (TENG) cannot maintain effective electrical output under high temperature conditions. In order to obtain high thermal charge stability, polyimide is modified with strong electron withdrawing groups like trifluoromethyl ($-CF_3$) and sulfone group ($-SO_2-$) in backbone. The fluorinated polyimides (F-PI) with a big band gap can provide a tribocharge density of 170 μC m^{-2} (4 times of common Kapton film) and become more negative than polytetrafluoroethylene in triboelectric series. In addition, $BaTiO_3$ nanoparticles are doped in F-PI film for inducing deep traps and interfacial polarizations for CE, which can further enhance the charge density (200 μC m^{-2}) and thermal charge stability. Finally, a flutter-driven TENG (FD-TENG) is designed based on this $BaTiO_3$-doped F-PI film to harvest wind energy and sense wind velocity. This FD-TENG can maintain 32% of its output performance at 200 °C in comparison with room temperature, which is the highest thermal charge stability reported for triboelectric polymers. Therefore, this $BaTiO_3$-doped F-PI has great application prospects for energy generation and motion detection in hot wind tunnel and many other harsh environments.

1. Introduction

Triboelectric nanogenerator (TENG), which is first proposed by Wang and co-workers in 2012,[1] is a promising technique to convert widespread mechanical energy in environment into electricity.[2] The fundamental working principle of TENG is based on the universal effect of contact electrification and electrostatic induction,[3] which gives the TENG the advantages of simple structure,[4] low cost,[5] small size, and high efficiency targeting at low-frequency energy source.[6] Meanwhile, the thermionic emission, which is an inevitable effect for almost all the triboelectric materials, is a crucial element that influences the fundamental mechanism of contact electrification.[7] Electrons transferred to the tribosurface during contact electrification can jump into vacuum because of thermal excitation, leading to the suppression of tribocharge generation and energy output of TENG. Moreover, triboelectric polymers may also lose their mechanical stability at high temperature environment, which may further decrease the effective output power of TENG. Triboelectric materials with high thermal charge stability are usually inorganic materials with low flexibility and low surface charge density. In this case, the application of TENG for high temperature conditions, including hot air sensor or energy package for harsh environment, may be severely limited, while the development of advanced triboelectric materials is key point for solving this problem.[8]

A series of previous works have been reported for improving the working temperature of TENG. For example, Ti and SiO_2 triboelectric layer and preannealing process have been used for rotating freestanding TENG, which can support the working condition of 400 °C.[9] In addition, some flame-resistant materials like polyimide yarn,[10] flame-retardant coat,[11] aerogel[12] are also reported to fabricate wearable TENG for fire escape and protection. TENG based on polytetrafluoroethylene (PTFE) also can maintain partial efficiency at 150 °C, while it generates little power above 200 °C.[13] On the other hand, polyimide (such as commercialized Kapton film) has been used for TENG due to its excellent triboelectric negativity and strong mechanical property.[14] Actually, a great number of monomers can be chosen to synthesize polyimide for tribolayer. For example, the triboelectric property of polyimide (PI) film can be further improved to succeed the performance of PTFE by designing its chemical structure[15] and transparent polyimide also has been synthesized for the application on screen surface.[16] Hence,

X. Tao, S. Li, Y. Shi, X. Wang, J. Tian, Z. Liu, P. Yang, X. Chen, Z. L. Wang
CAS Center for Excellence in Nanoscience
Beijing Key Laboratory of Micro-Nano Energy and Sensor
Beijing Institute of Nanoenergy and Nanosystems
Chinese Academy of Sciences
Beijing 100083, P. R. China
E-mail: chenxiangyu@binn.cas.cn
X. Tao, S. Li, Y. Shi, X. Wang, J. Tian, Z. Liu, P. Yang, X. Chen, Z. L. Wang
College of Nanoscience and Technology
University of Chinese Academy of Sciences
Beijing 100049, P. R. China
Z. L. Wang
School of Materials Science and Engineering
Georgia Institute of Technology
Atlanta, GA 30332-0245, USA

with the diversified monomers, the modified polyimides have the potential to achieve both high charge density and thermal charge stability. In addition to material selection, the mechanism study for quenching down thermionic emission in contact electrification is the fundamental approach for raising the working temperature of TENG and more efforts should be also devoted to this direction.[9]

In this work, we have synthesized two kinds of fluorinated polyimide (F-PI) films. These F-PI, with strong electron withdrawing groups in backbone, can provide a big highest occupied molecular orbital (HOMO)–lowest unoccupied molecular orbital (LUMO) gap with plenty of surface states for charge transfer. Hence, a tribocharge density of 108 and 170 μC m^{-2} is achieved with these two F-PI films, which is 2.5 and 4 times of that from Kapton film. Furthermore, BaTiO$_3$ nanofiller is doped in F-PI film to induce interfacial polarization and surface deep traps, which results in a triboelectric polymer with both high charge density and ultrahigh thermal charge stability. Then, a flutter-driven TENG (FD-TENG) is designed based on these F-PI to harvest wind energy under high temperature conditions. The nanocomposite F-PI film allows this FD-TENG to provide over 32% of its maximum output current at 200 °C, which is the highest thermal charge stability reported for triboelectric polymer. Thus, this FD-TENG has the potential to apply for self-powered sensor for hot steam and hot wind tunnel, also supplying a strategy to harvest environment energy in high temperature environment.

2. Results and Discussion

PI has excellent mechanical property, thermal stability, and flame retardancy, which is widely employed as negative triboelectric layer for TENG applications.[17] To further improve surface charge density and thermal charge stability of PI, strong electron-withdrawing groups like trifluoromethyl (−CF$_3$) and sulfone group (−SO$_2$−) are introduced to the main chain (see **Figure 1**a). In order to suppress the thermionic emission for improving thermal charge stability, our approach focuses on the change of chemical structure and the induced aggregation structure (Figure 1b). Here, three PI films are synthesized by step-growth condensation and thermal imidization, as reported.[18] At first, dianhydrides such as pyromellitic dianhydride (PMDA), 4,4′-(hexafluoroisopropylidene)phthalic anhydride (6FDA), and diamines like 4,4″-oxydianiline (ODA), bis(3-aminophenyl) sulfone (APS), and 2,2″-bis(trifluoromethyl)benzidine (TFDB) are polymerized in N,N-dimethylacetamide (DMAc) solvent to form polyamic acid (PAA) solution in N$_2$ atmosphere, respectively. After that, the PAA solution is cast onto a cleared glass plate and casting knife is used to control thickness, then cyclodehydration is carried out by heating at 100, 200, and 300 °C for 1 h under high vacuum. Then, PI films (PMDA–ODA, 6FDA–APS, and 6FDA–TFDB) are peeled off from substrate in clear water. The detailed chemical process and preparation method are presented in Figure S1 (Supporting Information) and the
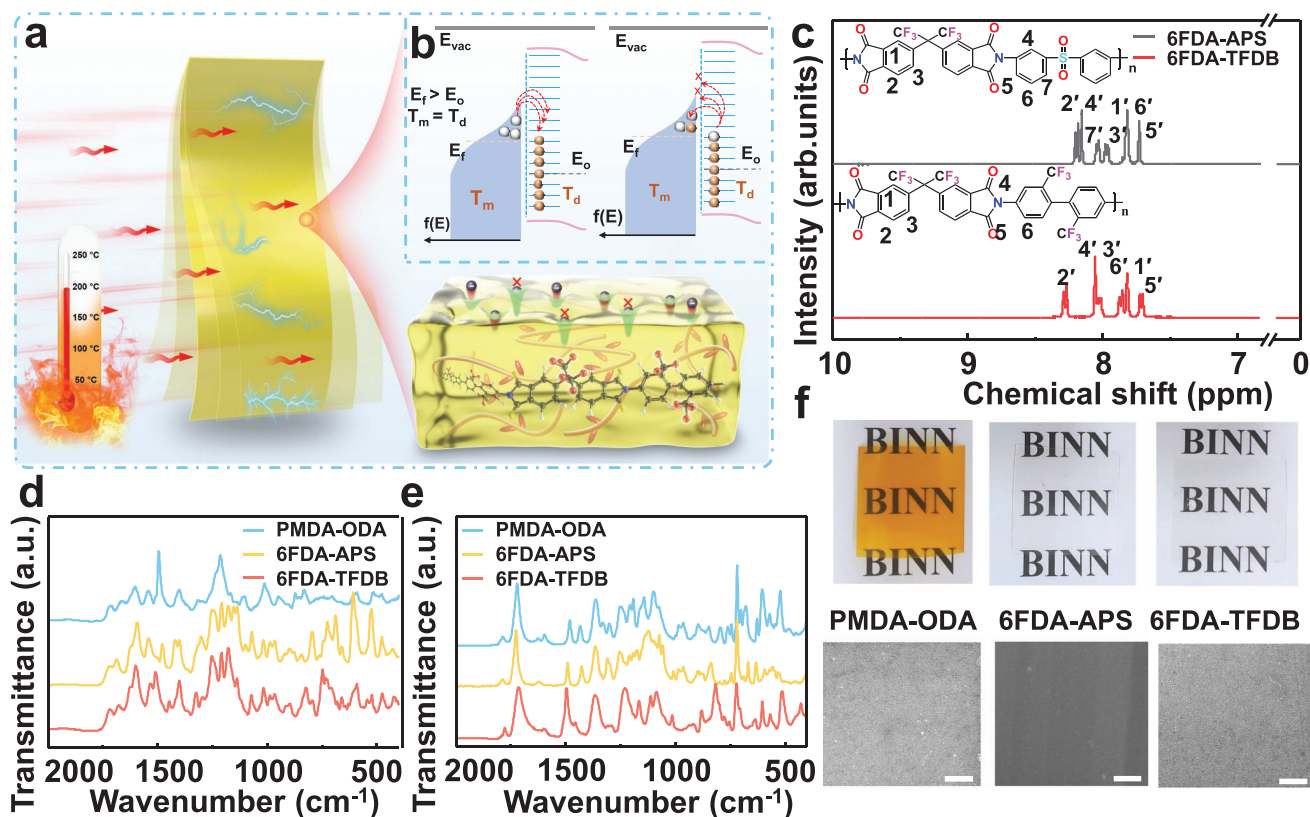

Figure 1. Schematic diagram and material characterization. a) Schematic to improve the charge stability of PI film at high temperature in molecular level. b) Schematic to obstruct effect of thermionic emission. c) ^{1}H NMR spectra and chemical structure of fluorinated PI films: 6FDA–APS, 6FDA–TFDB. d) FT-IR spectra of the three kinds of PAAs. e) FT-IR spectra of PI films. f) Photographs and SEM images of PI films (scale bars are 500 nm).

PI films used in this paper are prepared by similar method with the thickness of 50 μm.

The ^{1}H nuclear magnetic resonance (^{1}H NMR) and the total reflectance Fourier transform infrared (FT-IR) spectroscopy are used to certify the chemical structure of PI films. The attribution of peaks in ^{1}H NMR spectra are consistent with the chemical structure of PI, as shown in Figure 1c. The peak around 11.0 ppm (−NHCO−) in PAA (see Figure S2a in the Supporting Information) disappears in PI spectra because of the complete imidization. Moreover, the conversion of PAA to PI can be observed at FT-IR spectra (see Figure 1d,e) with the emergence of peaks at 1775 cm^{-1} (asymmetrical C=O stretch), 1718 cm^{-1} (symmetrical C=O stretch), and 1367 cm^{-1} (C−N stretch), and disappearance of peaks at 3100 cm^{-1} (O−H and N−H stretch) (see Figure S2b,c in the Supporting Information). In addition, the photograph and scanning electron microscope (SEM) of these PI films are shown in Figure 1f, which demonstrates that these PI films have similar surface roughness and surface morphology. Noting that, F-PI films (6FDA−APS, 6FDA−TFDB) are transparent due to the existence of strong electron-withdrawing group in backbone, which can suppress the charge transfer complex effect in PI films.[18]

The prepared F-PI films, after annealing at 200 °C to remove the residual surface charge and residual stress, contact with different materials to test their triboelectric performance and triboelectric series. According to our previous study,[19] the 6FDA−TFDB film, which contains four trifluoromethyl (−CF$_3$) groups per unit, may have the strongest electron-withdrawing ability. Hence, the 6FDA−TFDB film is first studied in **Figure 2**a. The charge density of 6FDA−TFDB film contacting with fluorinated ethylene propylene (FEP), PTFE, Kapton, polyvinyl chloride (PVC), polyethylene glycol terephthalate, and Al is summarized in Figure 2a, where the contact area is fixed to be 1×1 cm^2. The triboelectric series of 6FDA−TFDB film is between PTFE and FEP (as can be seen in Figure 2b with detailed value of transferred charge and current), which is more negative than Kapton, PVC, and other positive materials. The voltage and current are also consistent with this result (see Figure S3a,b in the Supporting Information). A transferred charge density around 30 μC m^{-2} and a current output of 1.2 μA are generated when the 6FDA−TFDB film contacts with FEP, while 35 μC m^{-2} and 1.0 μA are generated with PTFE. Therefore, the electrification capability of 6FDA−TFDB film is greatly improved comparing
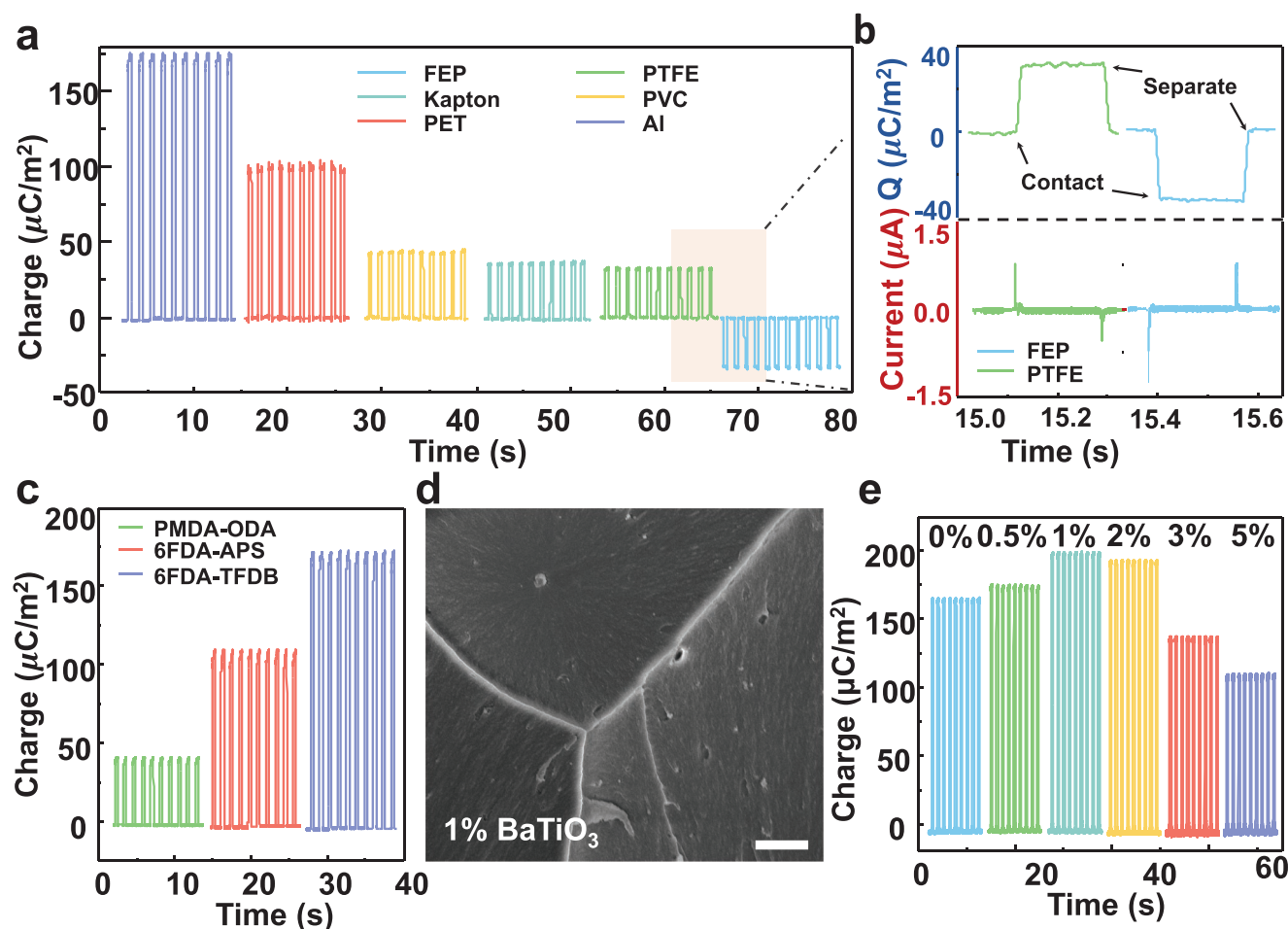

Figure 2. Triboelectric properties of PI films and BaTiO$_3$-doped 6FDA−TFDB. a) Triboelectric series of F-PI tested by charge density of 6FDA−TFDB contact with another dielectric. b) Amplified transferred charge and current of 6FDA−TFDB contact with FEP and PTFE. c) Charge density of three PI films contacted with Al. d) SEM image of cross-section of 1% BaTiO$_3$-composited PI, scale bar is 1 μm. e) Charge density of nanocomposite 6FDA−TFDB films with different mass fractions of BaTiO$_3$. All the contact area is 1×1 cm^2.

with Kapton. The charge density of PMDA–ODA, 6FDA–APS, and 6FDA–TFDB contact with Al is 42, 108, 170 $\mu C \, m^{-2}$, respectively (Figure 2c). The voltage and current generated by $1 \times 1 \, cm^2$ PI are also shown in Figure S3c,d (Supporting Information). Based on the result of Figure 2a,c, 6FDA–TFDB film has a maximum charge density of 170 $\mu C \, m^{-2}$ (4 times comparing with Kapton film).

To further enhance the triboelectric performance and thermal charge stability of 6FDA–TFDB, $BaTiO_3$ nanocomposite 6FDA–TFDB film is fabricated.[20] At first, the homogeneous PAA solution is synthesized by in suit polymerization of $BaTiO_3$ nanoparticle and monomers. Then, same process is operated to obtain 50 μm doped film with different filler proportions. In order to observe the dispersion of $BaTiO_3$ nanoparticle in substrate, the cross-section of doped 6FDA–TFDB film is observed by SEM. When the proportion of composite filler is less than1%, the filler has a good dispersion and no cluster or aggregation (see Figure 2d and Figure S4a,b in the Supporting Information). Meanwhile, the charge density of composited film is also enhanced in the case of proper amount of $BaTiO_3$ doping (Figure 2e). However, if the percentage of

$BaTiO_3$ nanoparticle is more than 2%, the generation of cluster and aggregation (see Figure S4c,d in the Supporting Information) may lead to the suppression of charge density (Figure 2e). Voltage and current outputs of 1×1 PI film containing $BaTiO_3$ filler are shown in Figure S4e,f (Supporting Information). Based on the result of Figure 2e and Figure S3 (Supporting Information), 1% $BaTiO_3$-doped 6FDA–TFDB film has a maximum charge density of 200 $\mu C \, m^{-2}$, which is almost 5 times than Kapton film. The doping concentration of 1% is quite small, which may be related to the high electrification capability of the F-PI film and the dispersion of $BaTiO_3$ nanoparticles.[21]

As the result of Figure 2a–c and Figure S2 (Supporting Information), the F-PI films that contain strong electron-withdrawing groups in main chain have visible enhancement of charge density and are more negative than PTFE in triboelectric series (**Figure 3**a). To study the effect of strong electron-withdrawing ($-CF_3$, $-SO_2-$) groups in backbone, density functional theory (DFT) calculations of chain element are analyzed. First, the electrostatic potential maps of structural units are shown in Figure 3b–d, where the blue and red regions are positive and negative potential regions, corresponding to the
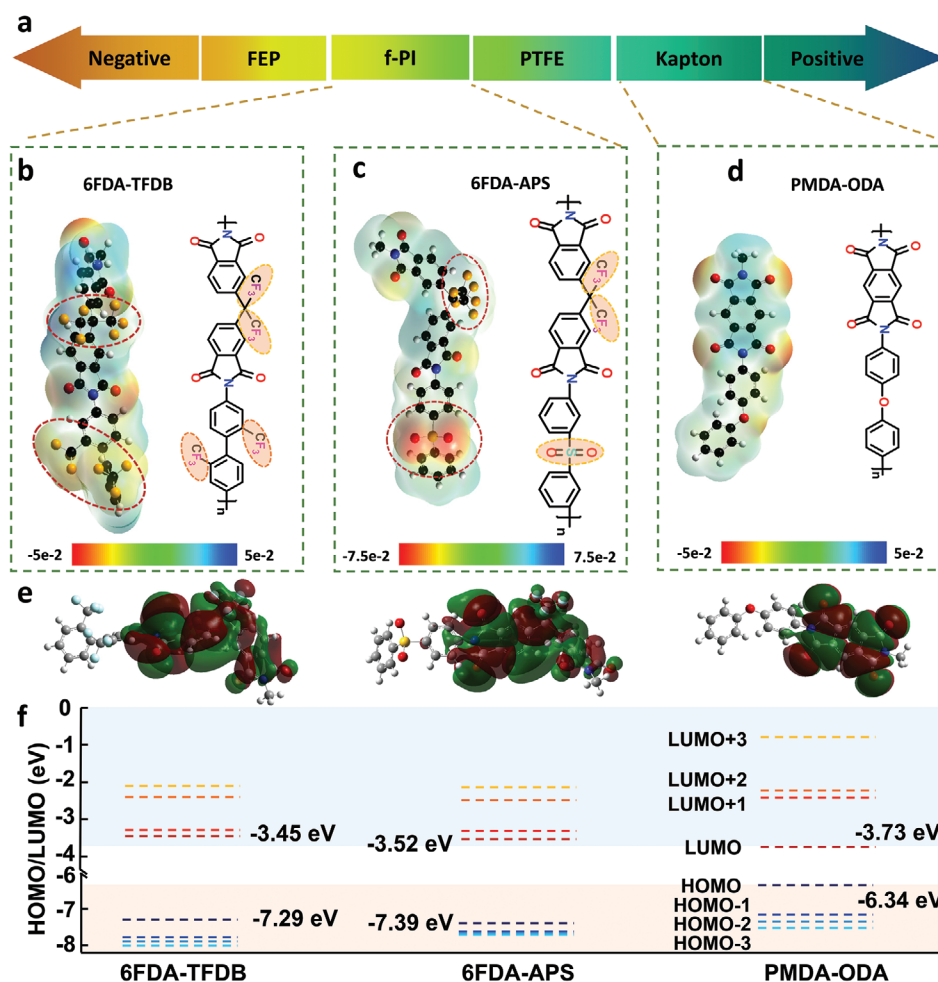

Figure 3. a) The position of different PI in triboelectric series. b–d) Electrostatic potential maps of PI: PMDA–ODA, 6FDA–APS, 6FDA–TFDB calculated using DFT simulations. e) LUMO distribution of the three PI films calculated using DFT simulations. f) Energy diagram of three monomers, of which energy levels are aligned with respect to vacuum energy level, between HOMO − 3 and LUMO + 3.

electron-poor and electron-rich regions, respectively. The red regions in PI, with robust ability to capture electron from the other electrode, distribute around the C=O in imide ring, ether ($-O-$), sulfone ($-SO_2-$), and trifluoromethyl ($-CF_3$) groups. Moreover, sulfone ($-SO_2-$) and trifluoromethyl ($-CF_3$) groups with huge steric hindrance also contribute to a big deflection of molecular configuration comparing with PMDA–ODA film. In addition, the LUMO of F-PI films (strong tendency of negative triboelectricity) also has certain extension (Figure 3e). The molecular orbital levels also calculate in Figure 3f, large LUMO–HOMO gap of F-PI can maintain more localized states for charge transfer. The gap of 6FDA–TFDB and 6FDA–APS is 3.84 and 3.87 eV, respectively, which is much larger than that of PMDA–ODA film (2.61 eV). It is worth noting that F-PI films have a dense orbital distribution in LUMO to LUMO + 3 and HOMO to HOMO − 3. The change of band structure caused by strong electron-withdrawing group may be the reason for the improvement of charge density. On the other hand, the interface between BaTiO$_3$ filler and surrounding polymers enhances the interfacial polarization and creates more electron deep traps.[22] The contribution of deep traps on the interface to the electrification is illustrated in Figure S5a,b (Supporting Information). The immigration and the relaxation of the tribocharges on the surface of F-PI lead to the charge accumulation on the interface between BaTiO$_3$ nanoparticles and PI film, which can be considered as a series of tiny capacitor to store the charges. Meanwhile, the charges captured by the deep traps[22] on the interface require higher excitation energy to escape (Figure S5c,d, Supporting Information). Therefore, both the surface charge density and the thermal charge stability of composited PI film are improved (Figure S5e,f, Supporting Information). However, too much filler may decrease the triboinduced charge density due

to the tunnel effect caused by filler cluster and aggregation.[23] Therefore, appropriate doping of F-PI is an effective strategy to improve charge density and charge stability.

Based on those fabricated PI films, an asymmetric FD-TENG is designed to harvest wind energy and sense wind speed at harsh conditions (**Figure 4**a). The 2D schematic with geometry parameters of FD-TENG is shown in Figure S6a (Supporting Information). The FD-TENG, the photo of which is shown in Figure S7c (Supporting Information), is made of two asymmetric Al electrodes and a flexible PI film. The arc-shaped Al electrode can manufacture turbulence in airflow, while the other flat electrode is for electrification with PI films. Therefore, turbulent airflow occurs as wind passes the arc-shaped Al electrodes, and then PI film shows reciprocating vibrations due to the actuation of turbulent airflow. The reciprocating vibrations of PI film results in the continuous contact–separation motion between film and Al electrode, leading to the generation of electrical signal. In this case, the length of PI film and cone angle of arc-shaped electrode, are the key factors affecting the motion of films, which should be further optimized to achieve the best structure parameters. As shown in Figure 4b and Figure S7a (Supporting Information), 8 cm PI film used here has the optimized output current, where film can flutter fast and strong. Long films, although have big contact area with electrode, are not beneficial for maintaining smooth motion (see Figure 4b and Figure S7d–f in the Supporting Information). The optimized cone angle of arc-shaped electrode is 45°, which is beneficial for the generation of turbulent (Figure 4c and Figure S7b (Supporting Information)). To observe the motion of the film, a high-speed camera records the vibrations image of the film, as shown in Movie S1 (Supporting Information). In addition, the potential distribution of scenarios is
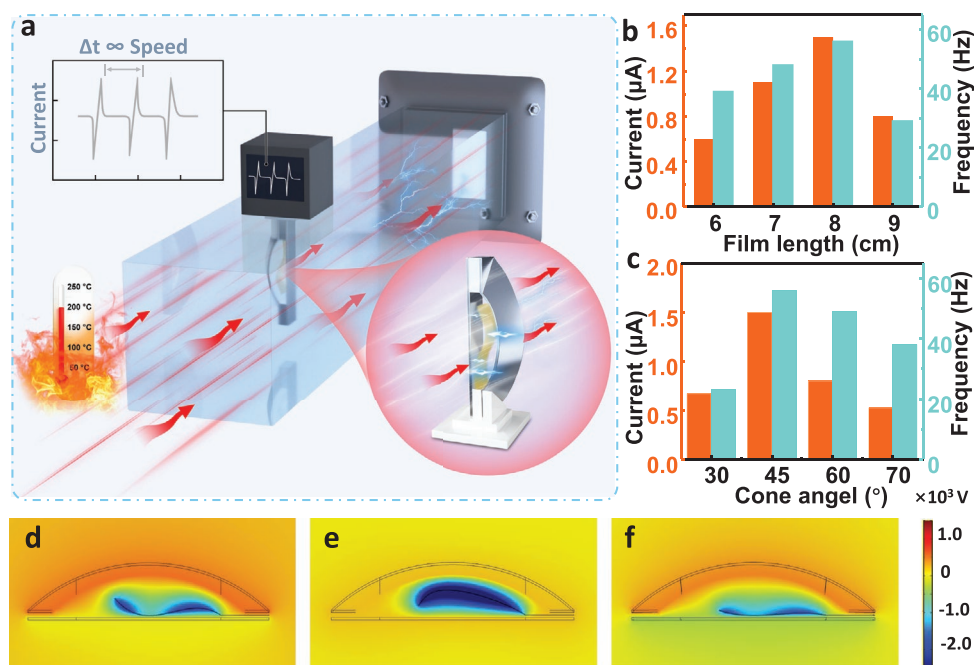

Figure 4. Device schematic and optimization. a) Schematic diagram of FD-TENG for wind energy harvesting and sensing at high temperature. b) Current magnificent and frequency of FD-TENG with 6FDA–TFDB flap for different PI film length. c) Current magnificent and frequency of FD-TENG with different angles of the cone. d–f) COMSOL simulation of potential map for FD-TENG with different states of flap during vibration.
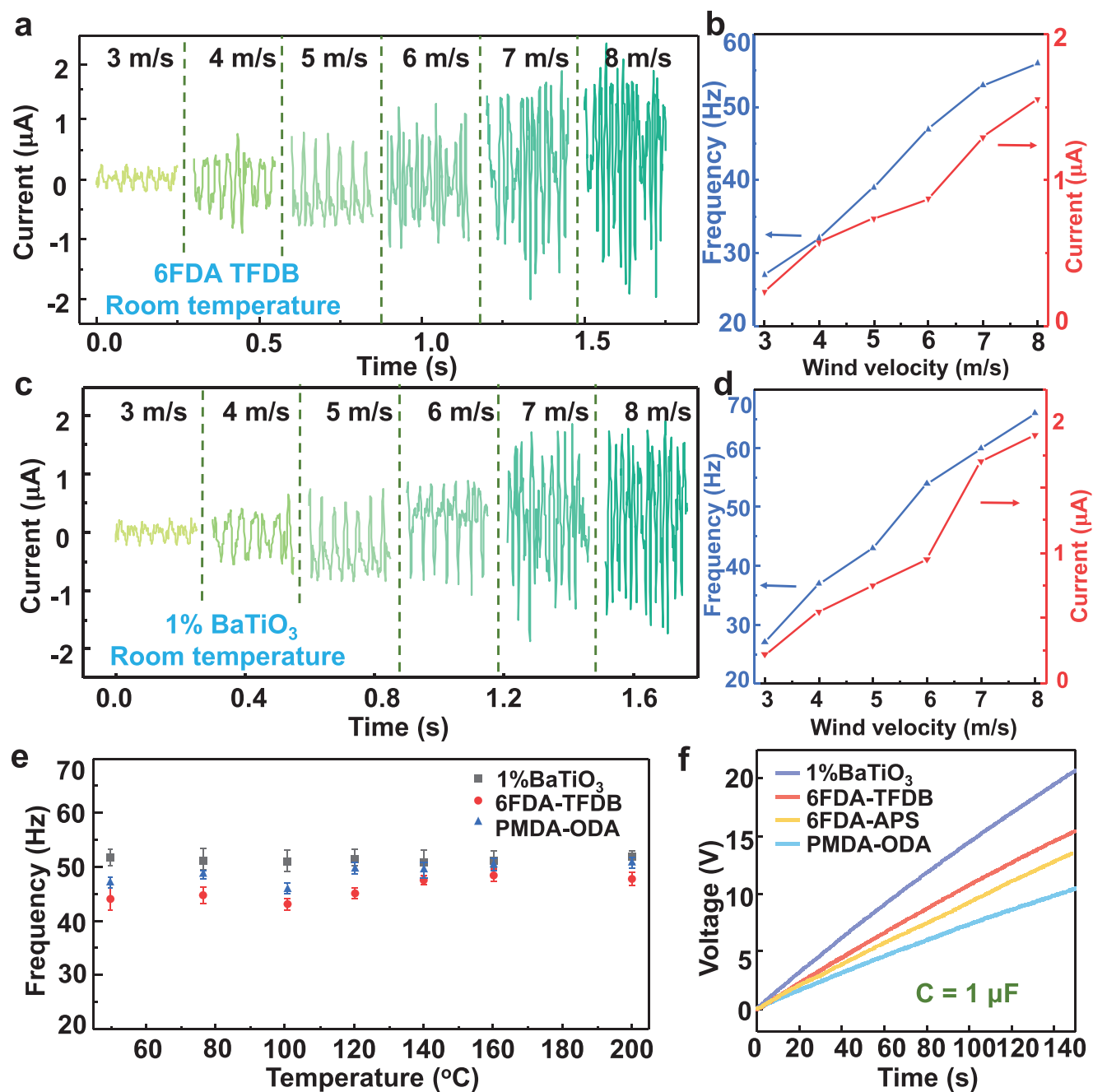
**ADVANCED
SCIENCE NEWS**

www.advancedsciencenews.com

**ADVANCED
FUNCTIONAL
MATERIALS**

www.afm-journal.de

Figure 5. Detecting wind speed by frequency of FD-TENG. Dependence of current induced by FD-TENG using a) 6FDA–TFDB flap or c) 1% BaTiO$_3$-doped 6FDA–TFDB film with wind velocity ranging from 3 to 8 m s^{-1}. Relationship between current magnificent and frequency of b) 6FDA–TFDB or d) 1% BaTiO$_3$-doped 6FDA–TFDB flap-based TENG and wind speed. e) Charging performance of the FD-TENG to a capacitor of 1 μF. f) The frequency of current at different temperatures with 6 m s^{-1} hot airflow.

also analyzed by finite-element simulation in Figure 4d–f. The potential of Al electrodes changes with the wave of film, and electron flow between the two electrodes due to contact electrification and electrostatic induction.

Performance of FD-TENG in room temperature is measured in a closed-loop wind tunnel control system, which can control wind velocity precisely. Obviously, the current of FD-TENG (based on 1% BaTiO$_3$-doped 6FDA–TFDB film) increases with the increase of airflow velocity from 3 to 8 m s^{-1}, as shown in

Figure 5a,c. Furthermore, the relationship between current magnitude (current frequency) and wind speed is also summarized at Figure 5b,d, respectively. At low wind speed like 3 m s^{-1}, the current is only 0.2 μA with a frequency less than 30 Hz. However, the magnitude and frequency both have noticeable increase with increased airflow velocity. The current of FD-TENG with pure 6FDA–TFDB film and 1% BaTiO$_3$-doped film can reach 1.52 μA, 56 Hz and 1.67 μA, 63 Hz in 8 m s^{-1} wind speed, respectively. Note that the frequency increases almost

linearly with the flow velocity and no response to temperature (Figure 5e), which can be used to detect wind speed. On the other hand, current magnitude may change with the ultrahigh temperature in harsh conditions, which can be used to reveal the temperature charge. In addition, the performance of different FD-TENGs to charge a 1 µF capacitor in 150 s is shown in Figure 5f, where the highest voltage of 20 V can be obtained on the capacitor by the FD-TENG (1% BaTiO$_3$-doped 6FDA–TFDB film).

At high temperatures, the output current of FD-TENG decreases due to the effect of thermionic emission. Here, the output current of FD-TENG based on different PI films is measured at 6 m s^{-1} hot airflow with different temperatures, and the temperature of devices is measured by a patch thermometer attached on Al electrode (Figure S6b, Supporting Information). The output performance of FD-TENG based on 6FDA–TFDB film has an obvious decay with the rising temperature (**Figure 6**b and Figure S8a,b (Supporting Information)) due to thermal stimulus. However, the current of FD-TENG with 6FDA–TFDB film is still more stable than that of FD-TENG with PMDA–ODA film (Figure 6a). This enhancement of triboelectric performance is the consequence of strong electron-withdrawing
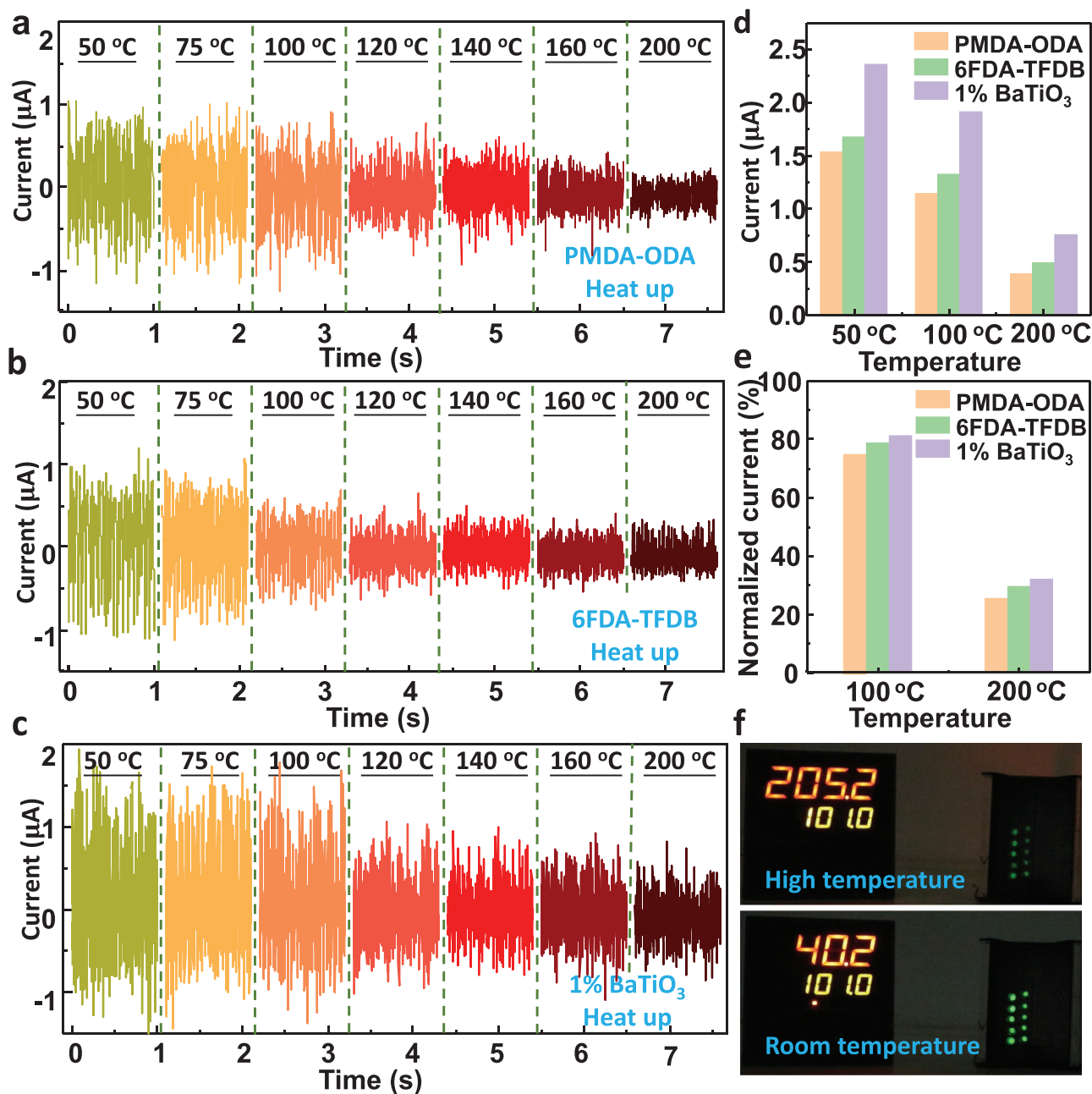

Figure 6. Detecting wind temperature by dependence of current magnificent and environmental temperature. The current of FD-TENG at 6 m s^{-1} hot airflow with a) PMDA–ODA, b) TFDB–6FDA, c) 1% BaTiO$_3$-doped 6FDA–TFDB flaps. The d) current and e) normalized current of FD-TENG at different temperatures. f) Photo of FD-TENG to light 10 LEDs at room temperature and 200 °C with 1% BaTiO$_3$-doped 6FDA–TFDB film.

groups in F-PI. Furthermore, the FD-TENG with 1% $BaTiO_3$-doped 6FDA–TFDB film has the biggest output current and the least attenuation in hot wind (Figure 6c). This result can be attributed to the deep traps induced on the interface between nanoparticle and surrounding polymer. The similar effect has been reported by the researchers in the field of dielectric materials,[21,22] while we demonstrated that the triboinduced charges can also be tightly attracted by these deep traps, leading to a stronger thermal charge stability. In addition, current and normalized current (I_T/I_{ROOM}) of FD-TENG with three kind of PI films are shown in Figure 6d,e and Figure S8c,d (Supporting Information). The current of FD-TENG has notable enhancement due to strong electron-withdrawing groups and $BaTiO_3$ doping. Moreover, the FD-TENG with 1% $BaTiO_3$-doped 6FDA–TFDB film has the largest normalized current at high temperature. Under 200 °C, the device can still maintain an output current of 0.7 µA (32% normalized current), which still can light 10 light emitting diodes (LEDs) (see Figure 6e and Movie S2 (Supporting Information)). The normalized voltage (Figure S8e, Supporting Information) and normalized charge (Figure S8f, Supporting Information) are also consistent with the result of Figure 5a–d. FEP, which is more negative than F-PI in the triboelectric series, is also used for fabricating FD-TENG device, in order to demonstrate the superior performance of F-PI. However, the mechanical property of FEP film is too soft for this kind of TENG and the output performance is rather weak in comparison with the devices using F-PI (see Figure S9a–d in the Supporting Information). In order to compare the thermal charge stability, the surface potential of FEP and F-PI at different temperatures has also been measured by using a Trek 347 noncontact electrostatic voltmeter (Figure S9e, Supporting Information). In the room temperature, contact electrification (rubbed with Al) can induce higher surface potential on the FEP surface, which is more significant than F-PI. However, at the high temperature above 100 °C, the surface potential of FEP film is sharply decreased and it returns to zero near 200 °C. Therefore, this 1% $BaTiO_3$-doped 6FDA–TFDB film has the highest thermal charge stability for triboelectric polymer at such high temperature, comparing with other reported polymers (Figure S10, Supporting Information).[8,13,24] The change of current magnitude at high temperature also can be used to detect the temperature of working environment, which can briefly show the change of the temperature. Therefore, this FD-TENG can be applied as the environmental energy harvester and self-powered sensor at high temperature environment, such as hot steam and airflow pipe.

3. Conclusion

In summary, we have synthesized F-PI films with high charge density and charge thermal stability by introducing strong electron withdrawing groups like trifluoromethyl (—CF_3) and sulfone (—SO_2—) into main chain. The charge density of 6FDA–TFDB film, which has a big LUMO–HOMO gap to contain more stable local states for electron transfer, can reach 170 µC m^{-2}, which is 4 times of that from common Kapton film. Moreover, $BaTiO_3$-doped 6FDA–TFDB film is also fabricated to further improve charge density (up to 200 µC m^{-2}) and

charge thermal stability by increasing electron deep traps and interfacial polarizations at interface. Using modified PI films, an asymmetric FD-TENG is designed to harvest wind energy and sense wind velocity at high temperature environment. Not only wind velocity can be detected by the frequency of film vibration, but also working temperature can be sensed by the magnitude of output current. In addition, the FD-TENG based on 1% $BaTiO_3$-doped 6FDA–TFDB film can still maintain 32% of its output performance at 200 °C comparing with room temperature, which is the highest thermal charge stability reported for triboelectric polymer. Therefore, this FD-TENG has potential to work as self-powered sensor at high temperature like hot steam and heat wind tunnel. Meanwhile, the synthesis process and the theoretical study of this $BaTiO_3$-doped 6FDA–TFDB film also provide a strategy to improve working temperature of triboelectric polymer.

4. Experimental Section

Materials: DMAc (AR) was purchased from Aladdin and vacuum distilled after drying over calcium hydride. $BaTiO_3$ (AR, about 100 nm), 6FDA, and PMDA were purchased from Aladdin. ODA, APS, and TFDB were purchased from Aladdin.

Synthesis Method: The polyimides were synthesized by two-step condensation polymerization. The first stage: the diamide and DMAc were added to the flask with vigorous stirrer, the flask was purged with flowing N_2. After diamide dissolved, an equimolar amount of dianhydride was then added. The mixed solution (solid content was 20%) was stirred vigorously at room temperature for 24 h to form homogeneous PAA solution. $BaTiO_3$-doped 6FDA–TFDB films were synthesized by in situ polymerization, appropriate $BaTiO_3$ nanofiller was added in DMAc, then ultrasonic dispersion was done for 0.5 h before adding the monomer. The second stage: the prepared PAA solution was blade coating on a flat precleaning glass substrate and then dried in 60 °C for 6 h, then heated at 100, 200, 300 °C for 1 h, respectively. After cooling down, the film was peeled off from glass substrate by immersion in water. At last, films were dried at 200 °C for 1 h at vacuum to anneal.

Measurements: ^1H NMR was performed in deuterated dimethyl sulfoxide, using a Bruker Avance 400 spectrometer. The total reflectance FT-IR spectra was measured with a VERTEX80v spectrophotometer. The surface morphology and cross-section of the film were observed using a Nova NanoSEM 450 field emission scanning electron microscopy. The electric generation was measured by 6514 electrometer (Keithley) and film contact was driven by a linear motor. Density functional theory calculations were applied on Gaussian 09 package with the nonlocal hybrid Becke three-parameter Lee–Yang–Parr function and the 6-311G. The surface potential was measured by a Trek 347 noncontact electrostatic voltmeter.

Fabrication of FD-TENG: The FD-TENG consisted of two Al electrodes and a PI film, one Al electrode was a 2 × 11 cm flat Al plate, the other was designed to be arc, as shown in Figure 3a, the PI film was in the middle of two Al electrodes and separated by PTFE spacer. The finite element analysis was applied on COMSOL, the surface charge density of PI film was -5×10^{-9} C. The opposite surface charge of Al electrode was calculated by integral PI surface and then evenly distributed up and down Al electrodes. The area of arc Al electrode was also obtained by surface integral.

Supporting Information

Supporting Information is available from the Wiley Online Library or from the author.

[1] a) F. R. Fan, Z. Q. Tian, Z. Lin Wang, *Nano Energy* **2012**, *1*, 328; b) S. Wang, L. Lin, Z. L. Wang, *Nano Lett.* **2012**, *12*, 6339; c) X. Song, Y. Chen, P. Li, J. Liu, F. Qi, B. Zheng, J. Zhou, X. Hao, W. Zhang, *Nanotechnology* **2016**, *27*, 30LT01.

[2] a) Y. Shi, F. Wang, J. Tian, S. Li, E. Fu, J. Nie, R. Lei, Y. Ding, X. Chen, Z. L. Wang, *Sci. Adv.* **2021**, *7*, eabe2943; b) C. Zhang, L. He, L. Zhou, O. Yang, W. Yuan, X. Wei, Y. Liu, L. Lu, J. Wang, Z. L. Wang, *Joule* **2021**, *5*, 1.

[3] a) Z. L. Wang, A. C. Wang, *Mater. Today* **2019**, *30*, 34; b) J. Nie, Z. Wang, Z. Ren, S. Li, X. Chen, Z. L. Wang, *Nat. Commun.* **2019**, *10*, 2264.

[4] a) Z. C. Quan, C. B. Han, T. Jiang, Z. L. Wang, *Adv. Energy Mater.* **2016**, *6*, 1501799; b) M. Y. Xu, Y. C. Wang, S. L. Zhang, W. B. Ding, J. Cheng, X. He, P. Zhang, Z. J. Wang, X. X. Pan, Z. L. Wang, *Extreme Mech. Lett.* **2017**, *15*, 122.

[5] a) Y. Yang, G. Zhu, H. Zhang, J. Chen, X. Zhong, Z. H. Lin, Y. Su, P. Bai, X. Wen, Z. L. Wang, *ACS Nano* **2013**, *7*, 9461; b) Z. Zhao, X. Pu, C. Du, L. Li, C. Jiang, W. Hu, Z. L. Wang, *ACS Nano* **2016**, *10*, 1780.

[6] a) Z. Ren, Z. Wang, Z. Liu, L. Wang, H. Guo, L. Li, S. Li, X. Chen, W. Tang, Z. L. Wang, *Adv. Energy Mater.* **2020**, *10*, 2001770; b) J. Bae, J. Lee, S. Kim, J. Ha, B. S. Lee, Y. Park, C. Choong, J. B. Kim,

Z. L. Wang, H. Y. Kim, J. J. Park, U. I. Chung, *Nat. Commun.* **2014**, *5*, 4929.

[7] a) S. Lin, L. Xu, C. Xu, X. Chen, A. C. Wang, B. Zhang, P. Lin, Y. Yang, H. Zhao, Z. L. Wang, *Adv. Mater.* **2019**, *31*, 1808197; b) C. Xu, Y. Zi, A. C. Wang, H. Zou, Y. Dai, X. He, P. Wang, Y. C. Wang, P. Feng, D. Li, Z. L. Wang, *Adv. Mater.* **2018**, *30*, 1706790.

[8] A. C. Wang, B. Zhang, C. Xu, H. Zou, Z. Lin, Z. L. Wang, *Adv. Funct. Mater.* **2020**, *30*, 1909384.

[9] C. Xu, A. C. Wang, H. Zou, B. Zhang, C. Zhang, Y. Zi, L. Pan, P. Wang, P. Feng, Z. Lin, Z. L. Wang, *Adv. Mater.* **2018**, *30*, 1803968.

[10] L. Ma, R. Wu, S. Liu, A. Patil, H. Gong, J. Yi, F. Sheng, Y. Zhang, J. Wang, J. Wang, W. Guo, Z. L. Wang, *Adv. Mater.* **2020**, *32*, 2003897.

[11] a) R. Cheng, K. Dong, L. Liu, C. Ning, P. Chen, X. Peng, D. Liu, Z. L. Wang, *ACS Nano* **2020**, *14*, 15853; b) H. F. Chen, C. Zhang, Y. C. Liu, P. Song, W. X. Li, G. Yang, B. Liu, *Rare Met.* **2020**, *39*, 498.

[12] Q. F. Zheng, L. M. Fang, H. Q. Guo, K. F. Yang, Z. Y. Cai, M. A. B. Meador, S. Q. Gong, *Adv. Funct. Mater.* **2018**, *28*, 1706365.

[13] a) C. X. Lu, C. B. Han, G. Q. Gu, J. Chen, Z. W. Yang, T. Jiang, C. He, Z. L. Wang, *Adv. Eng. Mater.* **2017**, *19*, 1700275; b) C. Rodrigues, M. Kumar, M. P. Proenca, J. Gutierrez, R. Melo, A. Pereira, J. Ventura, *Nano Energy* **2020**, *72*, 104682.

[14] S. Y. Li, Y. Fan, H. Q. Chen, J. H. Nie, Y. X. Liang, X. L. Tao, J. Zhang, X. Y. Chen, E. G. Fu, Z. L. Wang, *Energy Environ. Sci.* **2020**, *13*, 896.

[15] a) J. W. Lee, S. Jung, T. W. Lee, J. Jo, H. Y. Chae, K. Choi, J. J. Kim, J. H. Lee, C. Yang, J. M. Baik, *Adv. Energy Mater.* **2019**, *9*, 1901987; b) J. W. Lee, S. Jung, J. Jo, G. H. Han, D.-M. Lee, J. Oh, H. J. Hwang, D. Choi, S.-W. Kim, J. H. Lee, C. Yang, J. M. Baik, *Energy Environ. Sci.* **2021**, *14*, 1004.

[16] J. Wu, X. L. Wang, J. Y. He, Z. H. Li, L. Z. Li, *J. Mater. Chem. A* **2021**, *9*, 6583.

[17] A. Chen, C. Zhang, G. Zhu, Z. L. Wang, *Adv. Sci.* **2020**, *7*, 2000186.

[18] a) H. J. Ni, J. G. Liu, Z. H. Wang, S. Y. Yang, *J. Ind. Eng. Chem.* **2015**, *28*, 16; b) M. Hasegawa, *Polymers* **2017**, *9*, 520.

[19] S. Li, J. Nie, Y. Shi, X. Tao, F. Wang, J. Tian, S. Lin, X. Chen, Z. L. Wang, *Adv. Mater.* **2020**, *32*, 2001307.

[20] a) Z. M. Dang, Y. Q. Lin, H. P. Xu, C. Y. Shi, S. T. Li, J. B. Bai, *Adv. Funct. Mater.* **2008**, *18*, 1509; b) C. W. Beier, J. M. Sanders, R. L. Brutchey, *J. Phys. Chem. C* **2013**, *117*, 6958.

[21] a) F. Guo, X. Shen, J. Zhou, D. Liu, Q. Zheng, J. Yang, B. Jia, A. K. T. Lau, J. K. Kim, *Adv. Funct. Mater.* **2020**, *30*, 1910826; b) Y. Wang, W. Jie, C. Yang, X. Wei, J. Hao, *Adv. Funct. Mater.* **2019**, *29*, 1808118.

[22] a) S. Peng, X. Yang, X. Yang, S. Wang, Y. Zhou, J. Hu, Q. Li, J. He, *Adv. Mater.* **2019**, *31*, 1807722; b) Y. Zhou, C. Yuan, S. J. Wang, Y. J. Zhu, S. Cheng, X. Yang, Y. Yang, J. Hu, J. L. He, Q. Li, *Energy Storage Mater.* **2020**, *28*, 255; c) M. Kim, D. Park, M. M. Alam, S. Lee, P. Park, J. Nah, *ACS Nano* **2019**, *13*, 4640; d) Y. X. Chen, X. Chen, X. F. Zhang, Q. D. Shen, *ACS Appl. Energy Mater.* **2020**, *3*, 3665.

[23] a) L. Jin, X. Xiao, W. Deng, A. Nashalian, D. He, V. Raveendran, C. Yan, H. Su, X. Chu, T. Yang, W. Li, W. Yang, J. Chen, *Nano Lett.* **2020**, *20*, 6404; b) A. Yazdan, J. Z. Wang, B. K. Hu, W. S. Xie, L. Y. Zhao, C. W. Nan, L. L. Li, *Rare Met.* **2020**, *39*, 375.

[24] a) Y. F. Ding, Y. X. Shi, J. H. Nie, Z. W. Ren, S. Y. Li, F. Wang, J. W. Tian, X. Y. Chen, Z. L. Wang, *Chem. Eng. J.* **2020**, *388*, 124369; b) X. N. Wen, Y. J. Su, Y. Yang, H. L. Zhang, Z. L. Wang, *Nano Energy* **2014**, *4*, 150.